Aerospace Science and Technology 152 (2024) 109371

Contents lists available at ScienceDirect

Aerospace Science and Technology

journal homepage: www.elsevier.com/locate/aescte

Analysis of hovering flight stability of an insect-like flapping-wing robot in Martian condition

Khanh Nguyen [a], Giheon Ha [a], Taesam Kang [b], Hoon Cheol Park [a,*]

[a] Department of Smart Vehicle Engineering, Future Drone Center, Konkuk University, Seoul 05029, South Korea
[b] School of Mechanical and Aerospace Engineering, Future Drone Center, Konkuk University, Seoul 05029, South Korea

ARTICLE INFO

Communicated by Huihe Qiu

Keywords:
Hovering
Flight dynamics
Stability derivatives
Low-air-density
Low gravity
Computational fluid dynamics
Mars

ABSTRACT

In efforts to search for life-form on a planet other than Earth, many projects have been launched to measure and analyze the surface and atmospheric conditions on Mars. To extend the exploration of Mars, scientists have attempted to perform flight in the extremely thin air environment of Mars. Inspired by the successful controlled flight of NASA's Helicopter on Mars, in this work, we investigate the six-degrees-of-freedom hovering flight dynamics of an insect-like flapping-wing robot, called KUBeetle. To hover the KUBeetle on Mars, using the scaling ratios of air density and gravity on Earth and Mars, we have found that the flapping frequency should be about 113.48 Hz, which is 4.93 times faster than that on Earth, and the required lift on Mars is about 38% of that on Earth. The computational fluid dynamics (CFD) analysis suggests that the lift produced by the flapping wings at the frequency on Mars is close to that predicted by the scaling ratios. A series of simulations are used to compute the stability derivatives to complete the equations of motion. The eigenvalue and eigenvector analyses have identified one fast subsidence mode, one slow subsidence mode, and one divergence oscillation mode in the longitudinal and lateral motions on Mars, which are identical to those on Earth. The dynamic responses of the robot under three initial disturbances in the translational speeds indicate that due to the 94% smaller real part of the complex roots in the divergence oscillation modes of the longitudinal and lateral motions on Mars, the growth of flight disturbances is much slower than on Earth. Therefore, the KUBeetle is capable of hovering flight on Mars, since it has enough time to use the feedback controls to stabilize the system. This work can be used to support the studies of the flight control of flapping wing robots in the Martian atmospheric condition, and to generalize such flight control for other non-terrestrial applications in the atmospheres of other planets and/or their moons.

1. Introduction

To answer the question on whether life exists in the solar system other than on Earth, many projects for planetary explorations have been launched [1]. Most recent active space explorations have focused on Mars exploration, probably because the planet is more similar to Earth in size and environment than the others, and the most accessible planet from Earth. Mars exploration is not limited to orbital exploration, such as Odyssey, MRO, and Maven, but extends to surface explorations using successfully landed and deployed rovers, such as Spirit, Opportunity, Curiosity, and Perseverance [2]. Interestingly, the Perseverance rover also brought the Mars Helicopter, also known as Ingenuity, for the first flight exploration on Mars. On April 19, 2021, Ingenuity wrote a new flight history by demonstrating a successful controlled flight for forty seconds in the Martian atmosphere [3]. In the early 21st century, the National Aeronautics and Space Administration (NASA) launched projects to realize Martian atmospheric flight beginning with three options of fixed [4,5], rotary [6,7], and flapping-wing (FW) vehicles [8,9]. After research on them for about two decades, the final choice was the rotary-wing robot, due to the various design requirements on the Martian air vehicle, and the matured technology of rotary wings. Flight on Mars is very challenging because of the ultra-low air density in the atmosphere, which is about 1.55% of Earth's density at sea level [10]. For flight in the extremely low air-density environment, it is fortunate that the gravity on Mars is about 37.76% that of on Earth [10]. Considering the lower air-density and lower gravity conditions, to make the 1.8 kg Ingenuity fly on Mars, two sets of 1.2-meter diameter long, counter-rotating rotors need to be rotated about five times faster than on Earth.

* Corresponding author.
E-mail address: hcpark@konkuk.ac.kr (H.C. Park).

https://doi.org/10.1016/j.ast.2024.109371
Received 24 January 2024; Received in revised form 24 June 2024; Accepted 2 July 2024
Available online 6 July 2024

The concept of bioinspired flapping flight is also a strong candidate for Mars air exploration, since insects fly using unsteady aerodynamics that produce larger lifts than predicted by steady aerodynamics [11–15]. Even though the bioinspired FW robots are technically less mature than the rotary-wing vehicles in terms of design and control, significant progress has recently been made in understanding the unsteady aerodynamics [11–15] and flight dynamics [16–21] of insects, and their implementation in several insect-like tailless FW robots that can fly with independent power sources, such as the Nano-hummingbird [22], Robotic hummingbird [23], KUBeetle [24–31], Delfly Nimble [32,33], NUS–Roboticbird [34], and Purdue hummingbird [35,36]. Despite the recent progress, more intensive research seems required to realize FW flight on Mars. An interesting report on the flight of bumblebees flying at high elevations may provide an insight into FW flight in low-air-density conditions. Typically, bumblebees fly at altitudes widely ranging (233 to 4260) meters above sea level [37,38]. Even when they are relocated at a higher elevation of 9000 m, where the air density is 50% lower than that of their habitat at 3000 m, they can still fly [37]. In the low-air density environment, the flapping wings produce lower aerodynamic lift and drag, and the lower drag results in the increase in the flapping speed and stroke amplitude. Then, as the air becomes thinner, the faster flapping speed and larger stroke amplitude partially compensate for the reduction of lift. Thus, under the low-air density condition, wings may automatically flap faster to some degree, and partially compensate for the lift reduction, without spending more power.

Recently, Refs. [39,40] introduced a conceptual design of the Martian FW robot, Marsbee. The authors employed sinusoidal functions to approximate the wing kinematics of the Marsbee for their computational fluid dynamics (CFD) simulation framework. They suggested two feasible FW configurations where the wing areas are six and twelve times larger than the original area, while the flapping frequencies are about (26 and 60)% lower than that on Earth, respectively. Unfortunately, the proper experiments in the reports did not well support the suggestion. More recently, in an experimental work on force generation by FWs under a low-air-density environment, Tsuchiya et al. [41] presented the first take-off of a flapper in a high-altitude-air environment, which is equivalent to a 66% reduction of air density at sea level. The low air density was simulated by reducing air pressure inside a vacuum chamber. To compensate for the lower-lift generation due to the low air density, they used three times larger wings than the reference wings, instead of raising the flapping frequency. It is reported that the measured lift produced by FWs was about 0.14 N, which is sufficient to lift off the flapper weighing 0.12 N. Wang et al. [42] performed a numerical study to search for the wing design that can improve lift generation and flapping efficiency in an ultra-low-density atmosphere. They concluded that a flexible wing with high aspect ratio, fast-flapping speed, and small-stroke motion can produce 38% larger lift and 21% higher efficiency.

In general, these reports can be regarded as pioneering aerodynamics studies towards the FW flight in the Martian environment. However, to draw a feasible design of a Mars FW robot, we need to study the flight dynamics of FW robots considering the lower gravity and air density of Mars, as well as the aerodynamics of FWs. Since the dynamic flight stability analysis of locust by Taylor and Thomas [21], the framework using the standard equation of motion for an aircraft [43,44] has been widely used in the flight dynamic analysis of hovering FW insects [18,19,16,45,46]. The framework assumes that the flapping frequency is reasonably higher than the natural oscillatory frequencies of insects. In this case, an insect can be regarded as a rigid body with six degrees of freedom (three translations and rotations). The assumption allows the application of the standard equations of motion for an aircraft implementing the cycle-average forces and moments to insects and FW robots. A set of the linearized equations of motion (EoM) for a FW robot are established by the stability derivatives and system parameters, and the use of small perturbation theory. The stability derivatives included in the EoM are determined using the cycle-average aerodynamic forces and moments, which can be computed by several methods, such as experiment [21], quasi-steady aerodynamic model [47,48], and unsteady blade element theory [49]. However, these methods show their limitations in prediction of the outcomes. For example, Taylor et al. [21] conducted an experiment to analyze the stability of the desert locust, assuming that the pitch-rate derivatives are independent of the angle of attack (AoA). This means that all the pitch-rate derivatives with respect to AoA are zero in the analyses. As confirmed in [47], the magnitudes of forces computed by the quasi-steady models overpredicted those obtained from CFD results by about 20%. Meanwhile, the rotational force needs to be included in the quasi-steady model to obtain similar poles computed by the framework based on CFD in the lateral direction. Similarly, the mechanism of clap–fling in FW was not included in the unsteady blade element theory [49]. As revealed in Refs. [24,29], the clap–fling showed significant unsteady effects on the lift and drag generation during stroke reversals. Thus, these methods may inaccurately predict the aerodynamic forces and moments. As a result, some of the stability derivatives computed by the above-mentioned methods are inevitably inaccurate. For this reason, numerical methods, such as CFD, have been widely used to study the flight dynamics of FW robots more precisely [19,28,50–52].

We have been developing insect-inspired FW robots, called KUBeetles [25,26,31], which can perform hovering flights for 8.8 min with a flapping frequency from (17 to 23) Hz, mimicking beetle flight. Inspired by the recent successful flight of the Ingenuity on Mars, we pose the question: how can we make the KUBeetle fly on Mars? To design the KUBeetle–Mars, we first aim to keep the mass and all system parameters the same as those of the KUBeetle–S model flown on Earth [31]. For flapping flight on Mars, a higher flapping frequency is required to produce a sufficient lift due to the extremely low air density. In this case, the wings, transmission, and all joints need to be reinforced to endure larger inertial force and torque. Implementing such modifications while ensuring minimal mass increase, we may be able to build a flapping-wing robot for flight on Mars and test the same flapping-wing system under the Earth and Mars conditions, which are our future work. Until then, we assume that the same FW kinematics in non-dimensional time over a period can be generated with the current flapping system under low air density. The FW kinematics measured in the tethered test [31], which is not in a simple harmonic form unlike the assumption in Ref. [39], does not change much, even in the low-air-density environment. It is because the stroke amplitude is predetermined, and the passive maximum wing rotation is preset by constraining the trailing edge at the wing root in the KUBeetle design [26,31]. Due to these designs, the measured lift coefficients of the KUBeetle's wings showed only slight changes under the conditions of lower air densities varying (100 to 10)% of that of the sea-level air density on Earth [53], which indicates only slight change in the FW kinematics under low air density. The change can be minimized when wings are operated at a higher frequency. Furthermore, if the measured lift coefficient at the Martian air density condition becomes significantly different from those measured in Ref. [53] due to change in FW kinematics change, we may in the future modify the wing vein structures to make the lift coefficient similar. Under lower-air-density and faster-flapping-speed conditions, despite the predetermined stroke amplitude, the flapping wing may bend excessively due to higher inertial forces developed at stroke reversals. The wing bending can be minimized by increasing bending stiffness of the wing's leading edge and installing stoppers to limit the wing motions at the stroke reversals. Therefore, the assumption regarding the FW kinematics can be considered valid.

With the above-mentioned assumptions, in this study, we first search for the flapping frequency that can allow the KUBeetle to perform hovering flight on Mars. Then, through a series of CFD analyses using the ANSYS–Fluent software, we compute the aerodynamic forces and stability derivatives at the hovering condition. Finally, we analyze the hovering flight dynamic characteristics of the KUBeetle-Mars using the

eigenvalue analyses and compare them with those on Earth in Ref. [28], to identify any significant changes in the hovering stability on Mars.

This paper is organized as follows: Section 2 presents the conditions for Martian hovering, definitions of disturbed quantities, CFD modellings, and mesh convergence study, as well as the flow solver option. Section 3 compares the aerodynamic lift, drag, and pitching moment at the center of gravity (CG) on Earth and Mars, presents the stability derivatives in both longitudinal and lateral motions, specifies the natural modes of motion, identifies changes in the time responses of the FW robots on Mars, compared to those on Earth, and provides further discussion. Finally, Section 4 concludes the paper.

2. Materials and methods

2.1. Flapping frequency for Martian hovering flight and ranges of disturbance quantities

In this section, we find the flapping frequency required for the KUBeetle to perform a hovering flight and the magnitudes of disturbances for hovering stability analyses on Mars. The physical values of the atmospheric conditions such as air density, gravity, kinematic viscosity, and dynamic viscosity of Earth and Mars are presented in Table 1. The FW robot with the same mass, wing design, and system parameters is assumed to flap its wings with a faster speed to fly on Mars. The parameters listed in Table 2 are used for the final design of KUBeetle flown on Earth [31].

The flapping speed and frequency of the wings hovering on Mars can be predicted by balancing the relationship of weight and lift on Earth and Mars. Eqs. (1)–(3) are used to define the weights of the robot (W), lifts (L), and moments (M) produced by the wings on Earth and Mars, respectively, where the subscripts E and M stand for Earth and Mars, respectively. Note that the parameters appearing in Eqs. (1)–(3) are summarized in Tables 1 and 2.

$$\begin{array}{ll} \text{On Earth } (E) & \text{On Mars } (M) \\ W_E = mg_E & W_M = mg_M \end{array} \tag{1}$$

$$L_E = 0.5\rho_E C_l V_E^2 S \qquad L_M = 0.5\rho_M C_l V_M^2 S \tag{2}$$

$$M_E = 0.5\rho_E C_m V_E^2 S c_{mean} \qquad M_M = 0.5\rho_M C_m V_M^2 S c_{mean} \tag{3}$$

where m is the mass of the KUBeetle, S is the two-wing area, c_{mean} is the mean chord length, g_E and g_M are the gravity values of Earth and Mars, respectively, ρ_E and ρ_M are the air densities on Earth and Mars, respectively, C_l and C_m are the lift and moment coefficients, respectively, and V_M and V_E are the mean flapping speeds on Mars and Earth at the radius of gyration of the wing, respectively. For clarity, Table 3 presents the physical values of the FW models on Earth and Mars. Following that, the process to obtain these values is explained further in the text. As reported in Ref. [28], the mean flapping speed on Earth is defined as $V_E = 2\phi f_E r_2 = 6.46$ m.s^{-1}, where $r_2 = \sqrt{M_{2nd}/S_{1w}}$ is the radius of gyration of the wing (42.34×10^{-3} m), corresponding to 56% of the wingspan (R), M_{2nd} is the second moment of inertia, S_{1w} is the one-wing area, ϕ is the wingbeat amplitude (in rad), and f_E is the flapping frequency on Earth.

The ratios of the weight, lift, moment, and gravity on Mars to those on Earth are computed in Eq. (4), respectively, in terms of air density, flapping speed, and frequency. According to Refs. [41,54], the changes in aerodynamic characteristics of the FW are insignificant under various low air density conditions. Thus, the coefficients of lift and pitching moment of the wing are assumed to be unchanged. In addition, the mass of the robot and wing geometry (c_{mean} and S) remain identical.

$$\frac{W_M}{W_E} = \frac{L_M}{L_E} = \frac{M_M}{M_E} = \frac{g_M}{g_E} = \frac{\rho_M}{\rho_E}\left(\frac{V_M}{V_E}\right)^2 = \frac{\rho_M}{\rho_E}\left(\frac{f_M}{f_E}\right)^2, \tag{4}$$

where f_M denotes the flapping frequency on Mars. By solving the relationship between densities and gravitational forces, f_M is approximately 4.93 times of f_E. This means that the KUBeetle needs to flap its wings 4.93 times faster than flapping on Earth to hover in the Martian thin atmosphere (or $V_M = 4.93V_E$). Then, using Eq. (4), the mean flapping speed (V_M) and flapping frequency (f_M) on Mars are about 31.85 m.s^{-1} and 113.48 Hz, respectively.

To perform the stability analyses on Mars, we need to identify the ranges of disturbed quantities, which are based on those proven to be sufficiently small for linearizing the EoM of general FWs on Earth: 7% of the mean flapping velocity for the disturbed translational speed (ΔV_E), and 10% of the flapping frequency for the disturbed rotational speed (Δq_E) [18–20]. The disturbed translational speeds on Mars (ΔV_M) can be computed by Eq. (4) as follows, even for the changed speeds of ($V_E + \Delta V_E$) on Earth and ($V_M + \Delta V_M$) on Mars:

$$\frac{\rho_M}{\rho_E}\left(\frac{V_M}{V_E}\right)^2 = \frac{\rho_M(V_M+\Delta V_M)^2}{\rho_E(V_E+\Delta V_E)^2} = \frac{\rho_M}{\rho_E}\left(\frac{V_M}{V_E}\right)^2 \frac{\left(1+\frac{\Delta V_M}{V_M}\right)^2}{\left(1+\frac{\Delta V_E}{V_E}\right)^2}. \tag{5}$$

Therefore,

$$\left(1+\frac{\Delta V_M}{V_M}\right)^2 = \left(1+\frac{\Delta V_E}{V_E}\right)^2. \tag{6}$$

For small ΔV_M and ΔV_E,

$$\frac{\Delta V_M}{V_M} = \frac{\Delta V_E}{V_E}. \tag{7}$$

This means that the ratio of the disturbed translational speed to the mean flapping speed on Mars is equal to that on Earth, which is 7%. Therefore, the disturbed translational speed on Mars ΔV_M is 2.23 m.s^{-1}.

Table 1
Atmospheric conditions between Earth and Mars [10].

	Symbols	Units	Earth	Mars
Air density	ρ	kg.m^{-3}	1.225	0.019
Gravity	g	m.s^{-2}	9.8	3.7
Kinematic viscosity	ν	m^2.s^{-1}	1.46×10^{-5}	5.17×10^{-4}
Dynamic viscosity	μ	N.s.m^{-2}	1.79×10^{-5}	9.82×10^{-6}

Table 2
Morphological parameters of the KUBeetle flown on Earth [31].

	Symbols	Units	Values
Body mass	m	g	17.6
Distance of two flapping wing axes	d	mm	19.0
Flapping frequency	f_E	Hz	23.0
Local chord length at radius of gyration	$c(r_2)$	m	0.0265
Mean chord length	c_{mean}	m	0.025
Mean flapping velocity	V_E	m.s^{-1}	6.46
Moments of inertia about the x_b-axis	I_{xx}	kg.m^2	8.70×10^{-6}
Moments of inertia about the y_b-axis	I_{yy}	kg.m^2	7.94×10^{-6}
Moments of inertia about the z_b-axis	I_{zz}	kg.m^2	2.38×10^{-6}
Product of inertia for the zx plane	$I_{xz} = I_{zx}$	kg.m^2	-3.94×10^{-7}
Radius of gyration of the wing	r_2	m	42.34×10^{-3}
Second moment of inertia	M_{2nd}	m^4	3.37×10^{-6}
Two-wing area	S	m^2	3.76×10^{-3}
Wingbeat amplitude	ϕ	degree	190.0
Wing length	R	m	0.075

Table 3
Physical values of the KUBeetle on Earth and Mars.

	Symbols	Units	Earth	Mars
Flapping frequency	f	Hz	23	113.48
Flapping period	T	ms	43.48	8.81
Mean flapping speed	V	m.s^{-1}	6.46	31.85
Disturbed translational speed	Δu	m.s^{-1}	0.453	2.23
Disturbed rotational speed	Δq	rad.s^{-1}	2.30	11.35

Similarly, using the definition of moment in Eq. (3) and the relationship in Eq. (4), the disturbed rotational speed on Mars (Δq_M) can be derived as follows:

$$\frac{\rho_M}{\rho_E}\left(\frac{V_M}{V_E}\right)^2 = \frac{\rho_M(V_M+\Delta q_M l)^2}{\rho_E(V_E+\Delta q_E l)^2} = \frac{\rho_M}{\rho_E}\left(\frac{V_M}{V_E}\right)^2 \frac{\left(1+\frac{\Delta q_M l}{V_M}\right)^2}{\left(1+\frac{\Delta q_E l}{V_E}\right)^2}, \tag{8}$$

where l is the reference length to relate the disturbed rotational and translational speeds. For small disturbances of Δq_M and Δq_E,

$$\frac{\Delta q_M}{V_M} = \frac{\Delta q_E}{V_E}. \tag{9}$$

Since $V_M/V_E = f_M/f_E$ in hover,

$$\frac{\Delta q_M}{f_M} = \frac{\Delta q_E}{f_E}. \tag{10}$$

This indicates that the ratio of the disturbed rotational speed to the flapping frequency on Mars is the same as that on Earth, which is 10%. Hence, the disturbed rotational speed on Mars Δq_M is chosen as 11.35 rad.s^{-1}.

2.2. Wing kinematics

The wing kinematics used for the current simulations are the same as those reported in Ref. [28]. Since the details on how to measure and process the wing kinematics were reported elsewhere [28], here we just briefly explain how the coordinates and wing kinematics were defined. Fig. 1A describes the local and global coordinate systems fixed on the body of KUBeetle ($O_b x_b y_b z_b$) and on Earth or Mars ($O_p x_p y_p z_p$), respectively. The origin O_b is located at the center of gravity (CG), where $O_b y_b z_b$ is the lateral plane of symmetry, and $O_b x_b z_b$ is the longitudinal plane of symmetry. The x_b axis points backwards, y_b axis directs to the right, and the z_b axis points vertically upwards, being aligned with the body vertical axis. On the body axis, the CG was adjusted to be located at 75% of c_{mean} below the stroke plane (Oxy). The chosen CG position is within the stable range required for the 6-degree-of-freedom (six-DOF) dynamic flight stability of the hovering KUBeetle, in which its longitudinal and lateral motions can be stabilized using the pitching and rolling rate feedback controls, respectively, as reported in Ref. [55].

To describe the wing motion, Fig. 1B introduces the reference coordinate system $Oxyz$. The pivot point of the left wing located at the reference O is used to identify the flapping axis, whose distance from the longitudinal plane of symmetry, $d/2$, is 9.5 mm, where d is the wing distance shown in Fig. 1A. In the cross sections of the wing, the full rotation angle θ_f is the angle between the stroke plane and the full-chord line that connects the leading edge and trailing edge. Meanwhile, the middle rotation angle θ_m is the angle between the stroke plane and the mid-chord line that connects the leading edge and mid-chord point. The wing feather axis aligns with the leading-edge of the wing and moves in the stroke plane, and the acute angle between the feather and y-axes is referred to as the flapping angle (ψ). Fig. 1C–E display the measured (mea) and fitted (fit) wing kinematics, while Fig. 1F & G show the

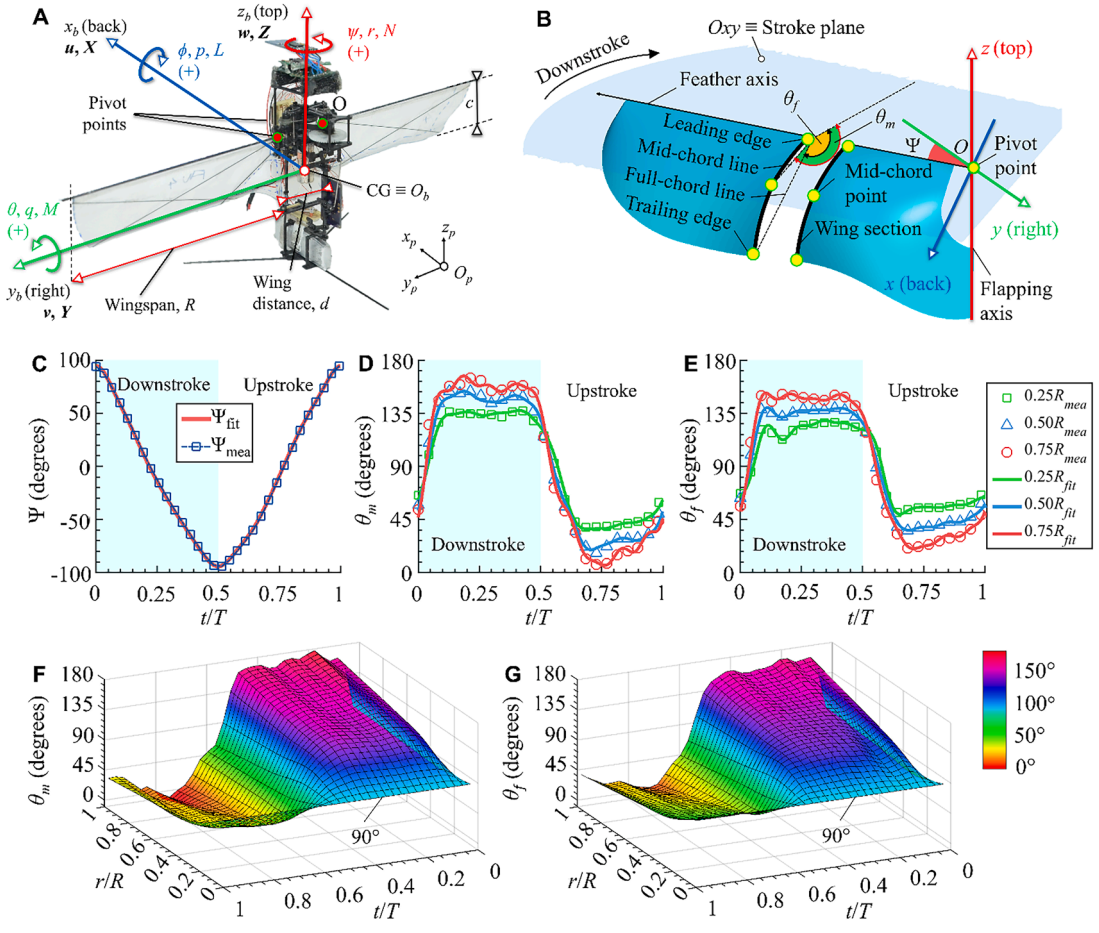

Fig. 1. Definitions of the coordinate systems and wing kinematics [28]. (**A**) and (**B**) Definition of the coordinate systems for (A) the KUBeetle with state variables of the translational velocities (u, v, w), rotational velocities (p, q, r), and body attitudes (ϕ, θ, ψ), and (B) the wing motion with the defined wing angles (α, θ_m, θ_f, ψ). (**C**)–(**G**) Wing kinematics: measured (mea) and fitted (fit) (C) flapping angles, (D) middle rotation angles, (E) full rotation angles at (25, 50, and 75)% R, and fitted (F) middle and (G) full rotation angles along wingspan with respect to the flapping cycle.

middle and full rotation angles along the wingspan over a flapping cycle. The fitted wing kinematics shown in Fig. 1C–E are used in the simulations as in Ref. [28]. More details on the measurement of wing kinematics can be found in Ref. [28].

2.3. Equations of motion (EoM)

Similar to the previous works [18,19,28,16,51,52,55,45], we use the linearized equations of motion and small perturbation theory. The effects of forces and moments produced by the FWs on the body can be represented by the cycle-average values. The techniques of eigenvalue and eigenvector analyses are used to obtain the natural modes of motion. Here, we briefly present the EoM, and the solutions of linearized EoM used for stability analyses. The longitudinal and lateral motions are characterized by the state variables of $[u,\ w,\ q,\ \theta]^T$ and $[v,\ p,\ r,\ \phi]^T$, respectively. The EoMs are linearized and shown in non-dimensional form for the longitudinal motion in Eq. (11), and the lateral motion in Eq. (12). Note that the symbol "δ" indicates a small perturbation quantity, the superscript "+" denotes the non-dimensional form of quantities, and the upper "." stands for the differentiation with respect to time (t^+).

$$\begin{bmatrix} \delta\dot{u}^+ \\ \delta\dot{w}^+ \\ \delta\dot{q}^+ \\ \delta\dot{\theta} \end{bmatrix} = \begin{bmatrix} \frac{X_u^+}{m^+} & \frac{X_w^+}{m^+} & \frac{X_q^+}{m^+} & g^+ \\ \frac{Z_u^+}{m^+} & \frac{Z_w^+}{m^+} & \frac{Z_q^+}{m^+} & 0 \\ \frac{M_u^+}{I_y^+} & \frac{M_w^+}{I_y^+} & \frac{M_q^+}{I_y^+} & 0 \\ 0 & 0 & 1 & 0 \end{bmatrix} \begin{bmatrix} \delta u^+ \\ \delta w^+ \\ \delta q^+ \\ \delta\theta \end{bmatrix}, \tag{11}$$

$$\begin{bmatrix} \delta\dot{v}^+ \\ \delta\dot{p}^+ \\ \delta\dot{r}^+ \\ \delta\dot{\phi} \end{bmatrix} = \begin{bmatrix} \frac{Y_v^+}{m^+} & \frac{Y_p^+}{m^+} & \frac{Y_r^+}{m^+} & -g^+ \\ \frac{L_v^+ I_z^+ + N_v^+ I_{xz}^+}{I_x^+ I_z^+ - I_{xz}^{+2}} & \frac{L_p^+ I_z^+ + N_p^+ I_{xz}^+}{I_x^+ I_z^+ - I_{xz}^{+2}} & \frac{L_r^+ I_z^+ + N_r^+ I_{xz}^+}{I_x^+ I_z^+ - I_{xz}^{+2}} & 0 \\ \frac{L_v^+ I_{xz}^+ + N_v^+ I_x^+}{I_x^+ I_z^+ - I_{xz}^{+2}} & \frac{L_p^+ I_{xz}^+ + N_p^+ I_x^+}{I_x^+ I_z^+ - I_{xz}^{+2}} & \frac{L_r^+ I_{xz}^+ + N_r^+ I_x^+}{I_x^+ I_z^+ - I_{xz}^{+2}} & 0 \\ 0 & 1 & 0 & 0 \end{bmatrix} \begin{bmatrix} \delta v^+ \\ \delta p^+ \\ \delta r^+ \\ \delta\phi \end{bmatrix}, \tag{12}$$

where the non-dimensional terms in the above system matrices are computed using Eqs. (13)–(21). The parameters used in these equations are listed in Tables 2 and 3. Forces in the x_b-, y_b-, and z_b-axes:

$$\begin{cases} X^+ = \dfrac{X}{0.5\rho_M V_M^2 S} \\ Y^+ = \dfrac{Y}{0.5\rho_M V_M^2 S} \\ Z^+ = \dfrac{Z}{0.5\rho_M V_M^2 S} \end{cases} \tag{13}$$

Roll, pitch, and yaw moments at the CG:

$$\begin{cases} L^+ = \dfrac{L}{0.5\rho_M V_M^2 S c_{mean}} \\ M^+ = \dfrac{M}{0.5\rho_M V_M^2 S c_{mean}} \\ N^+ = \dfrac{N}{0.5\rho_M V_M^2 S c_{mean}} \end{cases} \tag{14}$$

Translational velocities:

$$u^+ = \frac{u}{V_M},\ v^+ = \frac{v}{V_M},\ w^+ = \frac{w}{V_M}. \tag{15}$$

Angular velocities:

$$p^+ = \frac{p}{f_M},\ q^+ = \frac{q}{f_M},\ r^+ = \frac{r}{f_M}. \tag{16}$$

Longitudinal disturbances:

$$\delta\dot{u}^+ = \frac{\partial\delta u^+}{\delta t^+},\ \delta\dot{w}^+ = \frac{\partial\delta w^+}{\delta t^+},\ \delta\dot{q}^+ = \frac{\partial\delta q^+}{\delta t^+},\ \delta\dot{\theta}^+ = \frac{\partial\delta\theta}{\delta t^+}. \tag{17}$$

Lateral disturbances:

$$\delta\dot{v}^+ = \frac{\partial\delta v^+}{\delta t^+},\ \delta\dot{p}^+ = \frac{\partial\delta p^+}{\delta t^+},\ \delta\dot{r}^+ = \frac{\partial\delta r^+}{\delta t^+},\ \delta\dot{\phi}^+ = \frac{\partial\delta\phi}{\delta t^+}. \tag{18}$$

Moments of inertia about the x_b-, y_b-, and z_b-axes:

$$\begin{cases} I_x^+ = \dfrac{I_x}{0.5\rho_M V_M^2 S c_{mean} T_M^2} \\ I_y^+ = \dfrac{I_y}{0.5\rho_M V_M^2 S c_{mean} T_M^2} \\ I_z^+ = \dfrac{I_z}{0.5\rho_M V_M^2 S c_{mean} T_M^2} \end{cases} \tag{19}$$

Product of inertia for the Oxz plane:

$$I_{xz}^+ = \frac{I_{xz}}{0.5\rho_M V_M^2 S c_{mean} T_M^2}. \tag{20}$$

Mass, gravity, and time:

$$m^+ = \frac{m}{0.5\rho_M V_m S T_M},\ g^+ = \frac{g_M}{V_M f_M},\ t^+ = \frac{t}{T_M}. \tag{21}$$

The sets of $\left(X_u^+,\ X_w^+,\ X_q^+;\ Z_u^+,\ Z_w^+,\ Z_q^+;\ M_u^+,\ M_w^+,\ M_q^+\right)$ and $\left(Y_v^+,\ Y_p^+,\ Y_r^+;\ L_v^+,\ L_p^+,\ L_r^+;\ N_v^+,\ N_p^+,\ N_r^+\right)$ are the non-dimensional stability derivatives in the longitudinal and lateral motions, respectively. The entries in the first set are defined as changes in $(X^+,\ Z^+,\ M^+)$ – the front-and-backward and vertical forces in the x_b- and z_b-axes, and pitch moment at the CG, respectively, divided by the corresponding change in the linear and angular speeds in the longitudinal motion $(u^+,\ w^+,\ q^+)$, respectively. Those in the second set are changes in $(Y^+,\ L^+,\ N^+)$ – the sideward force in the y_b-axis, and the roll and yaw moments at the CG, respectively, divided by the corresponding change in the linear and angular speeds in the lateral motion $(v^+,\ p^+,\ r^+)$, respectively. The rotational angles (θ and ϕ) represent the attitudes of pitching and rolling Euler angles, respectively. The solutions of EoMs are expressed in Eq. (22) [21]:

$$\delta\mathrm{x}(t^+) = \mathbf{C}diag\left(\mathrm{e}^{\lambda_1 t^+}, \mathrm{e}^{\lambda_2 t^+}, \mathrm{e}^{\lambda_3 t^+}, \mathrm{e}^{\lambda_4 t^+}\right)\mathbf{C}^{-1}\delta\mathrm{x}(0), \tag{22}$$

where $\delta\mathrm{x}(t^+)$ represents the non-dimensional state vectors in the longitudinal motion $[\delta u^+,\ \delta w^+,\ \delta q^+,\ \delta\theta]^T$ and in the lateral motion $[\delta v^+,\ \delta p^+,\ \delta r^+,\ \delta\phi]^T$, $\mathbf{C}$ is a non-singular matrix whose columns are the eigenvectors of the system matrix, $\lambda_\mathrm{j} = n \pm \omega\mathrm{i}$ $(\mathrm{j} = 1, 2, 3, 4)$ are the corresponding eigenvalues, where n is the real part and ω is the imaginary part of the roots, and $\delta\mathrm{x}(0)$ is the initial conditions. If the $\delta\mathrm{x}(0)$ is selected as the eigenvector ϕ_j corresponding to the eigenvalue λ_j for the j^{th} mode, the motion of system can be shown for each of the j^{th} natural modes, as follows:

$$\delta\mathrm{x}(t^+) = \phi_\mathrm{j}\mathrm{e}^{\lambda_\mathrm{j} t^+}. \tag{23}$$

Section 3.3 presents the detailed analyses of the eigenvalues and eigenvectors.

2.4. Computational fluid dynamics modeling and result validation

Fig. 2A & B present the CFD models used in the analyses for the longitudinal and lateral motions, respectively. The similar meshing methods used in the previous works [24,27–29,55] are applied to model the computational domains with similar sizes. Two parameters (in millimeters) are used to identify the mesh size: the maximum edge length of the triangular elements on the wing surface, l_1, and the maximum edge length of the tetrahedral elements around the high-density region, l_2. From the previous work in Ref. [28], it was confirmed that the mesh with a pair of $(l_1 \times l_2) = (0.5 \times 2.0)$ mm^2 provided the conversed aerodynamic forces. Thus, we applied these two values to model the current CFD domains, corresponding to the half and full cylinders filled by 3.0 and 4.2 million grid cells, which are used for the longitudinal and lateral motion analyses, respectively. We also used the same time step size of 0.1% of a flapping period for the converged solutions, as in Ref. [28]. Thus, the results based on the current modeling can be regarded as converged solutions. More details on the meshing methods can be found in Refs. [24,27–29,55].

In addition, the local Reynolds number (Re) at the radius of gyration of the wing (r_2) is computed using Eq. (24), which is widely used to calculate the Re of a flapping wing [12,27–29]:

$$Re(r_2) = \frac{V_M c(r_2)}{\nu_M} = \frac{V_M c(r_2)\rho_M}{\mu_M}, \tag{24}$$

where $c(r_2)$ represents the local chord length at r_2, ν_M denotes the kinematic viscosity, μ_M stands for the dynamic viscosity, and ρ_M symbolizes the fluid density of the air on Mars. Based on the parameters in Table 1, the $Re(r_2)$ is 1635, which is about one seventh of $Re(r_2)$ of 11,744 on Earth. Thus, the air flow environment is regarded as laminar, and the laminar flow option is used for the current CFD analysis, as in the previous works [24,27–29,55]. For accuracy assurance, we compute the hovering lift and drag on Earth with the current longitudinal modeling as shown in Fig. 2A, and compare the results with those in Ref. [28]. In Fig. 2C & D, the time courses of the two lifts (in A) and drags (in D) in the second and third flapping cycles are almost identical. The cycle-average lift computed by the current mesh setting is 16.98 gf, which is about 0.7% larger than the computed one in Ref. [28]. Thus, the accuracy of the current CFD model is validated.

3. Results and discussion

3.1. Aerodynamic forces and pitching moment of Martian hovering flight

After the flapping frequency has been determined as 113.48 Hz for hovering flight of the KUBeetle on Mars, the lift, drag, and pitching moment produced by the FWs are computed, and compared with those produced on Earth, as shown in Fig. 3A–C, respectively. The tendencies of lift, drag, and pitching moment about the CG on Earth and Mars look similar, but the peaks of forces and pitching moment (M) are significantly lower in the Martian hovering condition (see Fig. 3A, B, & C, respectively), which results in considerable decreases in the cycle-average values. For example, the cycle-average lift and drag are about (5.99 and 5.11) gf, which are about (65 and 63)% lower than the (16.98 and 13.82) gf produced on Earth, respectively. In the pitching moment calculation, for the purpose of comparison with the published data in Ref. [28], the same CG location of the Earth FW design is used to compute the cycle-average M produced on Mars, without adjusting the x position of the CG on the longitudinal plane of symmetry to make the M perfectly zero as we did in previous works [28,52]. Because of that, the

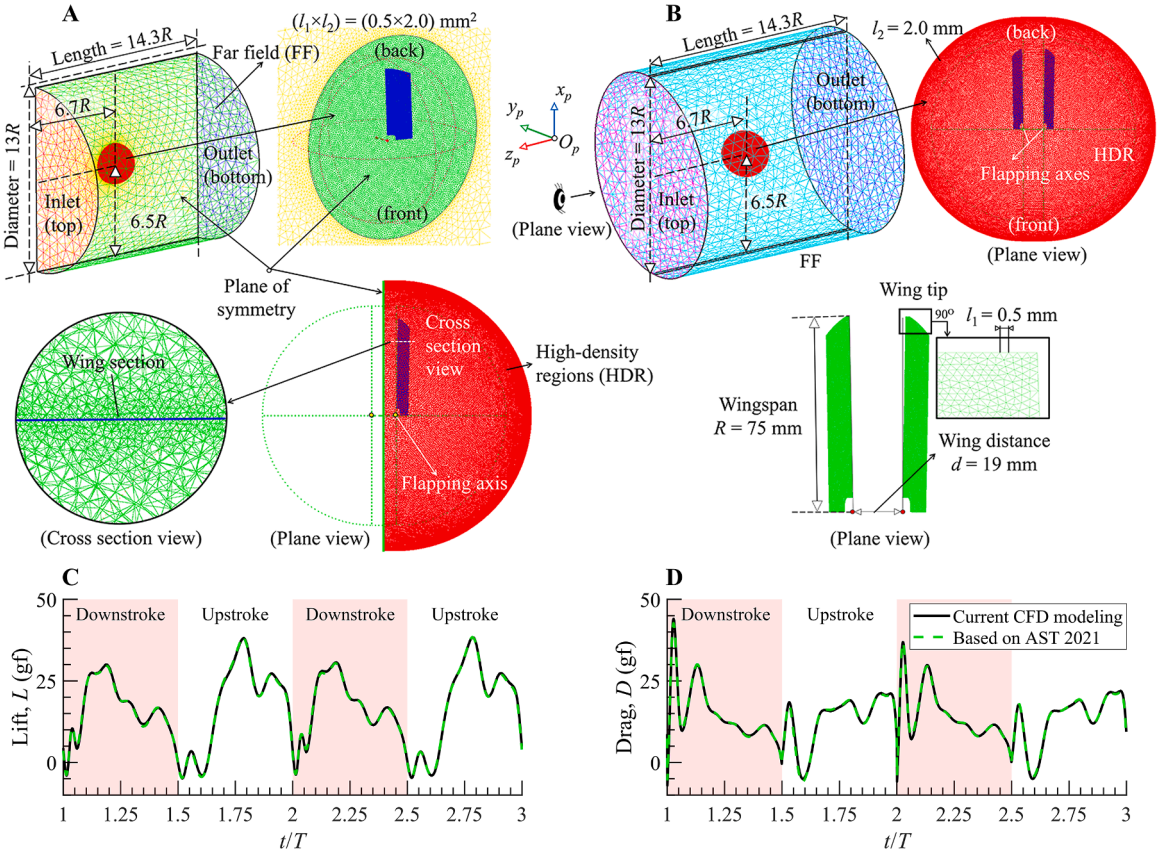

Fig. 2. CFD modeling and mesh convergence. (**A**) & (**B**) Mesh configurations of the computational domain, far field (FF), high-density region (HDR), and wing surface for the models used in the (A) longitudinal and (B) lateral analyses. (**C**) & (**D**) Comparison of (C) hovering lift and (D) drag on Earth over the second and third cycles (using the longitudinal mesh configuration) for the current CFD modeling and the previous one in Ref. [28], denoted by Based on AST 2021.

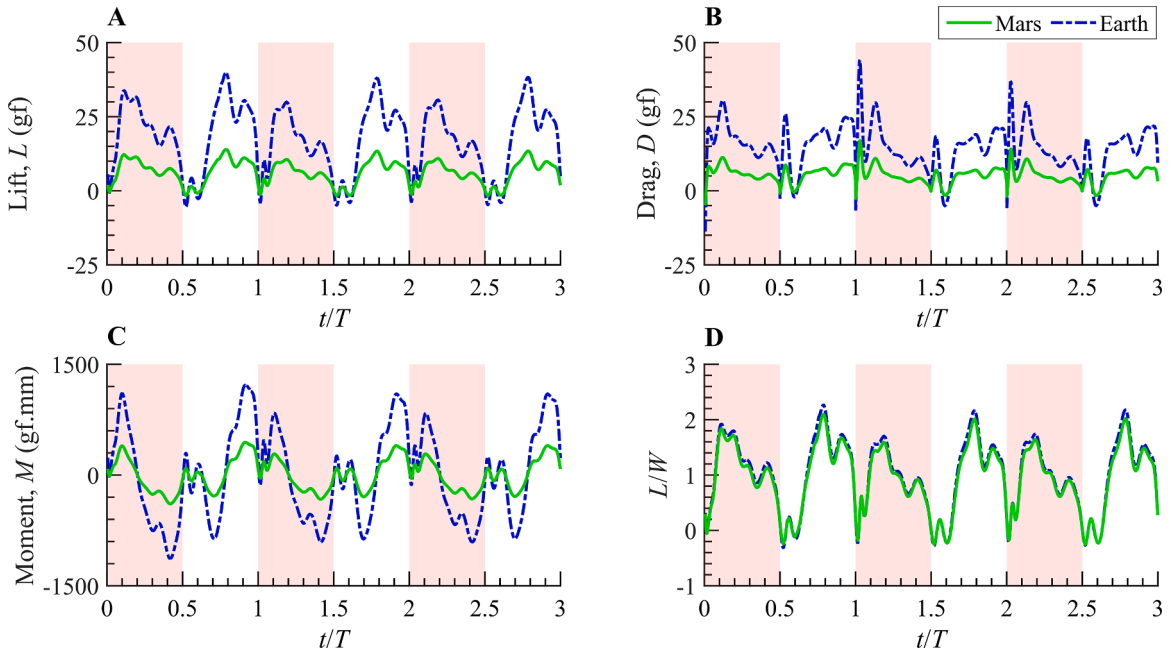

Fig. 3. Time courses of (A) lift, (B) drag, (C) pitching moment at the CG, and (D) normalized lift over three flapping cycles. The shaded areas represent the downstroke wing motions.

pitching moment M about the CG on Mars is not exactly zero, but is about -0.76×10^{-5} N.m. In addition, even using this same CG for the calculations on Earth, the M computed by the current CFD modeling is also non-zero, but is about 0.46×10^{-5} N.m. Therefore, the negligible pitching moments can be regarded as numerical errors raised by the different CFD modeling. This also interprets the difference of the small and insignificant non-dimensional stability derivatives, which are especially related to the terms of pitching, rolling, and yawing moments, as presented in Table 4. In addition, Fig. 3D shows the time course of normalized lift on Mars and Earth. Since the CFD calculation is based on the scaled flapping frequency, both time courses of normalized lift should be close to each other.

3.2. Stability derivatives

To obtain the stability derivatives on Mars, we first compute the cycle-average forces and moments produced in the perturbed motions, which can be treated as deviations from the reference hovering flight condition. Then, using the ranges defined for perturbed quantities in the translational (u, v, w-series) and rotational motions (p, q, r-series), stability derivatives can be calculated. For example, a stability derivative of Z_u^+, which is defined as the changes of vertical forces divided by the changes of translational speeds in the longitudinal motion (Δu_M^+) can be computed as follows:

$$Z_u^+ = \frac{Z^+\left(u_{M,e}^+ + \Delta u_M^+, w_{M,e}^+, q_{M,e}^+\right) - Z^+\left(u_{M,e}^+ - \Delta u_M^+, w_{M,e}^+, q_{M,e}^+\right)}{2\Delta u_M^+}, \tag{25}$$

where Z^+ is the non-dimensional cycle-average vertical force, $\left(u_{M,e}^+, w_{M,e}^+, \text{and } q_{M,e}^+\right)$ are fixed at zero as the values of the equilibrium flight, and $\Delta u_M^+ = 0.07$ is the small perturbation of the u-series derived by Eq. (7). Table 4A & B summarize the non-dimensional stability derivatives for the longitudinal and lateral motions in hover on Earth [28] and Mars, respectively. Note that the shaded columns in Table 4 indicate the major terms. The analyses on Mars show that the magnitudes of the major non-dimensional stability derivatives are close to the corresponding quantities on Earth. However, their dimensional values are only about (6 to 11)% of those on Earth (see Table A in Appendix). As revealed in Refs. [18,52,55], the sets of $(X_u^+, Z_w^+, M_u^+, \text{and } M_q^+)$ and $(N_r^+, L_p^+, L_v^+, \text{and } Y_v^+)$ show significant influences on the flight dynamics in the longitudinal and lateral motions of the FWs, respectively. Although the magnitudes of M_q^+ and L_p^+ are relatively small compared to the other major non-dimensional stability derivatives (Table 4A & B), the system poles are sensitive when their magnitudes are changed [28]. Meanwhile, the effects of the other derivatives on the system poles are insignificant, even though their magnitudes become significantly larger. These trends were confirmed in the study of the hovering flight of the KUBeetle on

Table 4
Non-dimensional (A) longitudinal and (B) lateral stability derivatives on Earth [28], and Mars.

(A)	Horizontal speed (u)-series			Vertical speed (w)-series			Pitch rate (q)-series		
	X_u^+	Z_u^+	M_u^+	X_w^+	Z_w^+	M_w^+	X_q^+	Z_q^+	M_q^+
Earth	−1.608	−0.071	−2.227	0.019	−0.899	−0.044	0.149	0.028	−0.059
Mars	−1.481	−0.082	−2.298	0.083	−1.035	0.074	0.134	0.020	−0.048
(B)	Yaw rate (r)-series			Roll rate (p)-series			Lateral speed (v)-series		
	L_r^+	Y_r^+	N_r^+	L_p^+	Y_p^+	N_p^+	L_v^+	Y_v^+	N_v^+
Earth	−0.077	0.059	−0.850	−0.054	−0.189	0.074	1.725	−1.803	0.254
Mars	0.034	0.036	−0.745	−0.080	−0.153	0.026	1.849	−1.681	0.154

Earth in Ref. [28]. More details on explaining the effects of all derivatives on the flight dynamics of the KUBeetle on Earth can be found in Ref. [28]. Since the major non-dimensional derivatives on Mars are close enough to the corresponding values on Earth, we expect that the system response is similar for the Martian hovering.

Fig. 4A–D & E–H show the changes of the non-dimensional forces and moments due to changes in the small ranges of disturbances, which are used to compute the first and second sets of the major non-dimensional derivatives of the longitudinal and lateral motions, respectively. In general, the tendencies and slopes of the non-dimensional forces and moments generated by small perturbations on Earth and Mars look similar. The fraction (Fr.) included in Fig. 4 stands for the ratio of each dimensional derivative on Mars to that on Earth, which are summarized in Table A in Appendix.

3.3. Eigenvalue and eigenvector analyses and natural modes of motion

Then, using the analyses of eigenvalues and eigenvectors in MATLAB [56], the flight dynamics of the KUBeetle hovering on Mars are characterized, and compared to those on Earth. The modes of motion are identified based on the magnitude and sign of the roots (eigenvalues) obtained from the system matrices, which are determined by the non-dimensional derivatives and system parameters, in the EoM for the longitudinal and lateral motions, as shown in Table 5A & B, respectively. Meanwhile, the plots in Fig. 5 illustrate the changes of root loci obtained from the 6-DOF motions on Earth and Mars. As revealed, the roots of the longitudinal and lateral motions on Mars include one fast subsidence mode (represented by a negative real root with a relatively larger magnitude), one slow subsidence mode (represented by the other negative real root with smaller magnitude), and one divergence oscillation mode (represented by a pair of complex conjugate roots in the right-half complex plane), which are similar to the flight modes defined on Earth [28]. However, their magnitudes are significantly smaller, compared to those obtained on Earth (in Table 5 and Fig. 5). This indicates that the effects of different gravity and density on the roots obtained from the EoM (in non-dimensional form) are significant.

The growth of the disturbance quantities is the exponential of the real part of the eigenvalues (n) and time (t) in Eq. (22). If the n is positive and small, the divergence oscillation modes are less dynamically unstable, while if the n is negative and small, the subsidence modes can be stabilized much more slowly. This means that with the small magnitudes of the eigenvalues of the flight on Mars, the times for the two subsidence modes of FW to be stabilized are longer than those on Earth. In addition, the speed for the divergence oscillation modes to increase due to disturbances is much slower than the mode on Earth. In Table 6, the detailed analyses are shown with the reference times of t_{half} and t_{double}, which present number of flapping cycles (or time) to halve the perturbations in the two subsidence modes and to double the perturbations in the divergence oscillation modes, respectively. In addition, when the initial disturbances are chosen as the eigenvector ϕ_j corresponding to the j^{th} natural mode, the time responses of each mode defined by Eq. (23) on Earth and Mars are graphically illustrated in Figs. A and B in Appendix for the longitudinal and lateral motions, respectively.

For example, in the fast subsidence longitudinal motion on Mars (Table 6A), since the magnitudes of the roots are about 94% smaller than that on Earth (see Table 5A), the initial disturbances are halved after 24.8 flapping cycles, corresponding to 0.22 s. This is about 3.15 times longer than 0.07 s, corresponding to 1.5 flapping cycles on Earth (see the non-dimensional time t_{half} in the fast subsidence mode in Table 6A). Similarly, the slow subsidence longitudinal mode on Mars needs 10.38 s, as 1,179 flapping periods are required to reduce the initial disturbances by a half, which is about 11.3 times longer than 0.92 s or 21.1 flapping periods on Earth. Meanwhile, since the magnitudes of the imaginary and real parts of the complex roots are relatively small (Table 5A), the period of the divergence oscillation longitudinal mode ($T_{mode} = 263.2$ flapping cycles or 2.32 s) on Mars, in Table 6A, is about 3.3 times longer than on Earth ($T_{mode} = 16.4$ flapping cycles or 0.71 s). Thus, the initial disturbances in the unstable oscillation mode become double after 0.46 s, corresponding to 51.9 flapping cycles (see t_{double} in Table 6A, Mars). This is about 2.9 times longer than the time for the robot to tumble on Earth, which is estimated to be after about 0.16 s, corresponding to 3.7 flapping periods. Similar tendencies occur for the lateral modes on Mars, in comparison with those on Earth. See Tables 5B & 6B.

3.4. Comparative flight dynamics of the hovering KUBeetle on Mars and Earth

This section compares the dynamic behaviors, including the displacements and attitude angles, of the KUBeetle deviating from the reference hovering condition on Earth (Fig. 6A1–C1) and Mars (Fig. 6A2–C2). For this purpose, the three initial perturbations, such as δu^+, δw^+, and δv^+ in the x_b-, y_b-, and z_b-axes, are considered, respectively. The non-dimensional initial perturbations of $\delta u^+(0)$, $\delta w^+(0)$, and $\delta v^+(0)$ are set to 0.07 in Fig. 6A–C, respectively, while the other corresponding non-dimensional initial disturbances are fixed at zero: ($\delta w^+ = \delta q^+ = \delta\theta = 0$), ($\delta u^+ = \delta q^+ = \delta\theta = 0$), and ($\delta p^+ = \delta r^+ = \delta\phi = 0$). Using Eq. (22) and the eigenvalues and eigenvectors in Section 3.3, the solutions of flight speeds and attitude angles, which are obtained

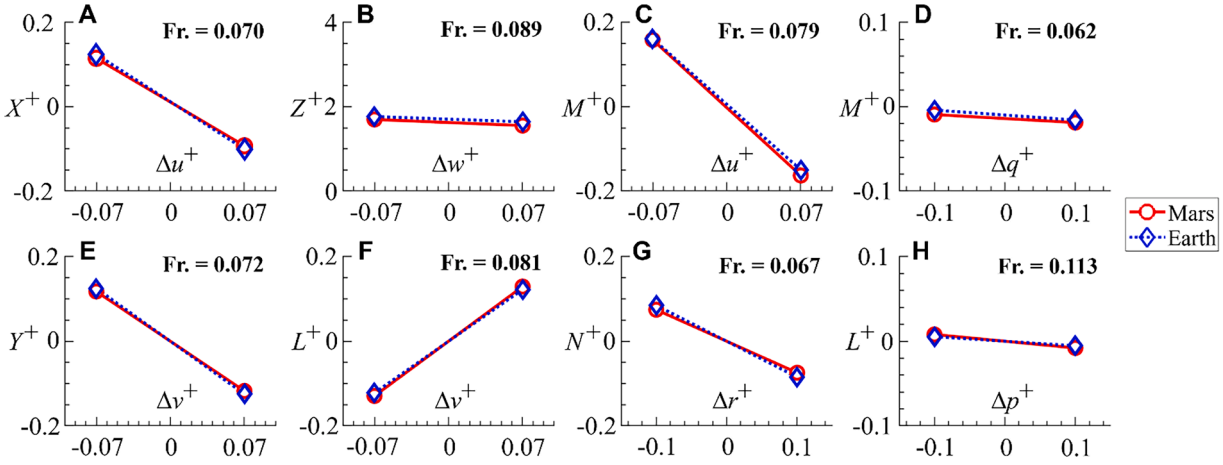

Fig. 4. Non-dimensional forces (X^+, Y^+, Z^+) and moments (L^+, M^+, N^+) due to non-dimensional small perturbed translational and rotational speeds explaining the production of four major stability derivatives in **(A)**–**(D)** the longitudinal motion, and **(E)**–**(H)** the lateral motion on Mars relative to those on Earth. Note that the abbreviation "Fr." stands for the ratio of each dimensional derivative on Mars to that on Earth.

Table 5
Roots (eigenvalues) of the characteristic equations in the (A) longitudinal and (B) lateral modes on Earth [28] and Mars.

		Fast subsidence (stable) ($\lambda_1 = n \pm 0i$)	Slow subsidence (stable) ($\lambda_2 = n \pm 0i$)	Divergence oscillation (unstable) ($\lambda_{3,4} = n \pm \omega i$)
(A)	Earth	−0.4643	−0.0328	0.1858 ± 0.3834i
	Mars	−0.0280 (−94 %) from Earth	−0.0006 (−98 %) from Earth	0.0133 ± 0.0239i (−94 %) from Earth
(B)	Earth	−1.6370	−0.4173	0.1598 ± 0.3402i
	Mars	−0.0249 (−99 %) from Earth	−0.0229 (−95 %) from Earth	0.0119 ± 0.0215i (−94 %) from Earth

(Note) The differences shown in the divergence oscillation modes of the Martian flights are computed by the magnitudes of the complex roots and their counterparts of the flights on Earth.

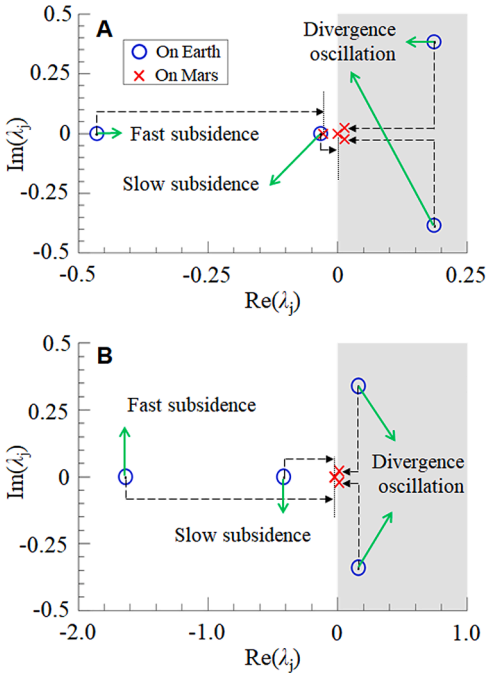

Fig. 5. Root loci for the (A) longitudinal and (B) lateral motions on Mars (denoted by crosses) and Earth (denoted by circles) [28]. Note that the dashed lines with arrows show shifts of the roots, the shaded areas in the right-half complex planes represent the unstable zones, the white left-half planes represent the stable areas, and the horizontal and vertical axes stand for the real and imaginary parts of the eigenvalues, respectively.

from the linearized EoM in the longitudinal and lateral motions, are computed during the first 0.5 s. Then, using the trapezoidal time integration rule [57] with a time step size of 5×10^{-4} s, corresponding to (1.2 and 5.7)% of the flapping cycles for the calculations on Earth and Mars, respectively, the horizontal, lateral, and vertical displacements are computed by integrating the flight speed components in the x_b-, y_b-, and z_b-axes, respectively. For example, the dimensional horizontal displacement, x, is computed by the dimensional horizontal flight speed, $\delta u(t)$, in the x-axis using Eq. (26), as follows:

$$\mathrm{x} = \int_{t_1}^{t_N} \delta \mathrm{u}(t)dt = \frac{t_N - t_1}{\mathrm{N}} \left(\sum_{\mathrm{k}=2}^{\mathrm{k}=\mathrm{N}-1} \delta \mathrm{u}(t_k) + \frac{\delta \mathrm{u}(t_N) + \delta \mathrm{u}(t_1)}{2} \right), \tag{26}$$

where $t_1 = 0$ stands for the time of the hovering reference flight, $t_N = 0.5$ s is the investigated time, which is regarded as long enough for the delay of feedback control on Earth [51], $N = 1000$ is the number of trapezoids, and $\delta u(t_k)$ is the flight speed at t_k. Note that the non-dimensional solutions obtained from the EoM need to be expressed in the dimensional forms for this analysis. As mentioned in Section 2.1, since $V_M = 4.93V_E$, the perturbed translational speeds on Mars are 4.93 times larger than those on Earth ($\delta u_M/\delta u_E = \delta v_M/\delta v_E = \delta w_M/\delta w_E = 4.93$). Therefore, within the same period, larger displacements deviating from the reference conditions on Mars are expected than on Earth. In detail, Fig. 6 demonstrates the position [x, y, z] of the pivot point of the right wing, and the Euler angles of $[\phi, \theta, \psi]$ of the body around the CG after the vehicle deviates from the hovering flight due to translational perturbances.

For example, Fig. 6A1 & 2 illustrate the dynamic responses of the KUBeetle under the initial backward perturbed speeds on Earth and Mars, which correspond to $\delta u_E(0) = 0.07V_E = 0.45$ m.s^{-1} and $\delta u_M(0) = 0.07V_M = 2.23$ m.s^{-1}, respectively. Under the disturbance, the displacements in the y- and z-axes, and the rolling and yawing rotation angles around the x_b- and z_b-axes, respectively, are almost negligible for flights on Earth and Mars. However, in Fig. 6A1, after flying backward (in the positive x_b direction) for the first 0.2 s from the hovering reference flight, the robot on Earth shows a forward motion (in the negative x_b direction) with a horizontal displacement of about 0.25 m (or –248.7 mm in Fig. 6A1) at $t = 0.5$ s. In contrast, when the body is disturbed and flies with a speed of 2.23 m.s^{-1} on Mars, the KUBeetle flies backward with a horizontal displacement of about 0.92 m (or +918.2 mm in Fig. 6A2). The robot on Mars monotonically increases the nose-down pitching angles for the first 0.5 s (see Fig. 6A2). Especially for the pitching moment from (0.4 to 0.5) s, corresponding to 11.3 wingbeats, the pitching angle increases to 120.6° Meanwhile, on Earth, an extreme nose-up angle of about 100° in pitch is reached at $t = 0.5$ s after 2.3 wingbeats due to the pitching moment at 0.4 s, when the robot flies with

Table 6
Reference times for each mode of motion in the (A) longitudinal and (B) lateral directions on Earth [28] and Mars.

		Period	Fast subsidence (stable)		Slow subsidence (stable)		Divergence oscillation (unstable)			
		T (ms)	$t_{half} = ln2\times\lvert\mathrm{Re}(\lambda_1)\rvert^{-1}$		$t_{half} = ln2\times\lvert\mathrm{Re}(\lambda_2)\rvert^{-1}$		$T_{mode} = 2\pi/\omega$		$t_{double} = ln2\times\lvert\mathrm{Re}(\lambda_{3,4})\rvert^{-1}$	
(A)	Earth	43.48	1.5	(0.07 s)	21.1	(0.92 s)	16.4	(0.71 s)	3.7	(0.16 s)
	Mars	8.81	24.8	(0.22 s)	1,178.8	(10.38 s)	263.2	(2.32 s)	51.9	(0.46 s)
(B)	Earth	43.48	0.4	(0.02 s)	1.7	(0.07 s)	18.5	(0.80 s)	4.3	(0.19 s)
	Mars	8.81	27.8	(0.25 s)	30.3	(0.27 s)	292.2	(2.57 s)	58.3	(0.51 s)

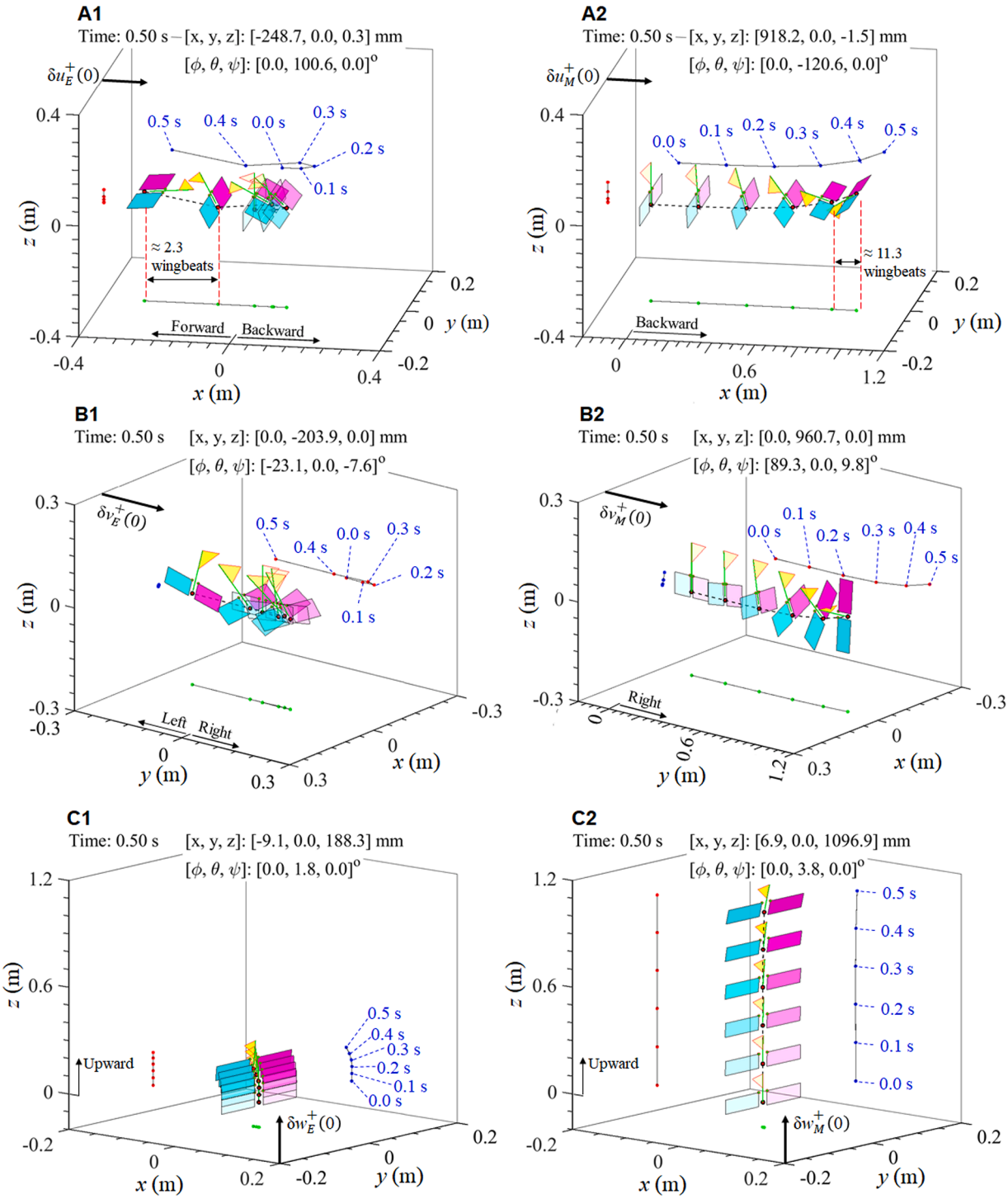

Fig. 6. Flight dynamics of the robots on Earth (**A1**, **B1**, & **C1**) and Mars (**A2**, **B2**, & **C2**) under the initial disturbances deviating from the hovering flight of (A1 & A2) $\delta u^+(0) = 0.07$, (B1 & B2) $\delta v^+(0) = 0.07$, and (C1 & C2) $\delta w^+(0) = 0.07$. Note that the yellow triangles indicate the front of the robot, the green lines stand for the vertical body axes (z_b), the surfaces with the cyan and magenta colors stand for the left and right wings, respectively, the red circles between two wings denote the CG, the solid lines with circles projected on the orthogonal planes represent the motion tracking of the CG, and the coordinates [x, y, z] in each plot mean the location of the pivot point of the right wing at $t = 0.5$ s measured from the pivot point at $t = 0$.

a nose-down pitching angle of 20° (Fig. 6A1). This indicates that the pitching motion about the y_b-axis of FWs on Earth is too fast compared to that on Mars, which may cause the system to quickly tumble. Since the solutions in Eq. (22) are the exponential function of eigenvalues and time, the positive and smaller real parts of the complex roots on Mars, which are about 93% smaller than those on Earth (see Table 5A & B for the unstable oscillation modes), results in less disturbed motions, in comparison with those on Earth at the same time t. In addition, the investigated time of the first 0.50 s corresponds to (11.5 and 56.8) flapping cycles on Earth and Mars, respectively, which are about (70 and 20)% of the first cycle of the divergence oscillation modes (T_{mode}) in the longitudinal motion on Earth and Mars, respectively (comparing with T_{mode} of (16.4 and 263.2) cycles in Table 6A, respectively). The analysis also shows that the initial disturbances in the longitudinal motion on Earth and Mars become double after (3.7 and 51.9) flapping cycles, corresponding to (0.16 and 0.46) s, respectively (see t_{double} in Table 6A). Therefore, as time goes by, the flight perturbation experienced on Earth increases significantly compared to that on Mars due to the relatively larger eigenvalues obtained on Earth in comparison to Mars. Overall, this analysis clarifies how the KUBeetle experiences the more rapid change from the nose-down to nose-up motions on Earth than on Mars, when the FW system is subjected to a small-perturbed transitional speed in the front-to-back direction. Similar interpretations can be applied to the lateral motion based on T_{mode} and t_{double} in Table 6B.

Fig. 6B1 & 2 graphically show the dynamic behaviors of the robot when the body is disturbed by a lateral wind blowing from left to right with a non-dimensional speed of $\delta v^+(0) = 0.07$, corresponding to (0.45 and 2.23) m.s^{-1} on Earth and Mars, respectively. On Earth (Fig. 6B1), the robot flies to the right for the first 0.2 s, then to the left for a distance of 0.2 m at $t = 0.5$ s. In addition, the body attitude angle changes from a positive value to −23.1° in roll during the time from (0.4 to 0.5) s, respectively (Fig. 6B1). Meanwhile, during the first 0.5 s on Mars, the rolling angle monotonically increases to 89.3° from the hovering reference flight, and the body moves towards the right for a distance of 0.96 m (see Fig. 6B2). Both plots show that the FWs fly with relatively small yawing angles on Earth and Mars, corresponding to (7.6 and 9.8)° at $t =$ 0.5 s, respectively. In addition, for these two flight conditions, the displacements in the vertical (z_b) and horizontal (x_b) axes are less significant than in the lateral axis, and the pitching rotations are decoupled from the disturbed motion by the small speed of δv.

With the initial non-dimensional disturbed vertical speeds of $\delta w^+(0)$ in the positive z_b-axis, the dynamic responses of the FW vehicles flying on Earth and Mars are described in Fig. 6C1 & 2, respectively. As depicted, they maintain a stable upward flight, and achieve altitudes of (0.188 and 1.097) meters within the initial 0.5 s flights with relatively small displacements of about 9 mm forward and about 7 mm backward motions on Earth and Mars, respectively. The plots show the relatively small pitching angles of (1.8 and 3.8)° for the flights on Earth and Mars, respectively, which are close to vertical flights. Meanwhile, the lateral translation, and rolling and yawing angles are decoupled from the disturbed vertical motions for both flight conditions.

3.5. Further discussions on CFD modeling validation and wing-kinematics assumption

Instead of providing details on convergence tests for mesh and time step size, we applied the same CFD modeling technique that we used in our previous publications. Still, we may need to discuss the accuracy of current CFD results. Fig. 2C and D can be a proof of converged solutions by the current CFD calculations. Using the same FW kinematics, the current CFD modeling nicely reproduced the time courses of lift and drag presented in our previous CFD calculations in [28]. Therefore, the cycle-average lift of 16.98 gf obtained by the current CFD modeling shows only 0.7% difference from that acquired in [28], as stated in Section 2.4. Thus, the current CFD for the on-Earth condition is already validated. In addition, Fig. 3D can be a proof of converged solution on Mars. The time course of normalized lift on Mars is close to that on Earth. Since the CFD calculation is based on the scaled flapping frequency, both time courses of normalized lift should be close to each other. Thus, the current CFD results can be regarded as converged solutions.

In this work, we have assumed that the FW kinematics are identical for hovering flights on Earth and Mars, which is a limitation of the current work. However, the assumption is inevitable until the actual FW kinematics on Mars are available. Similarly, in [39], the authors used a set of assumed FW kinematics on Mars for their CFD analyses. When we can design and successfully fabricate the KUBeetle-Mars, another CFD based on the measured actual FW kinematics will be performed and compared with the current work. Thus, the current CFD result can be used as a reference solution and for identifying change of aerodynamic forces due to the change in the FW kinematics.

Under faster-flapping-speed conditions for flight at extremely low density, like on Mars, wings and transmissions need extra reinforcement because they have to endure larger inertial forces. Therefore, instead of just increasing flapping frequency and keeping the wing geometry, enlarging wing area and lowering flapping frequency is another option for flight on Earth. Indeed, the KUBeetle could record endurance of about 8.8 min due to installing enlarged wings, which lowered the required flapping frequency [26]. Thus, we may have another design strategy instead of just increasing flapping frequency for flapping flight under extremely low air density, as described in [39,41].

4. Conclusions

By scaling the weights and lifts, and assuming the constant lift coefficients of the flapping wings under low air density, the required hovering flapping frequency on Mars of the KUBeetle is identified to be 113.48 Hz, which is 4.93 times faster than on Earth. The 6-DOF flight dynamics of the FWs in the low-density and low-gravity environment of Mars are investigated through a series of CFD simulations. The stability derivatives are computed by taking into account the effects of small perturbations on aerodynamic forces and moments. The methods of eigenvalues and eigenvectors are used to analyze the state variables, including the three components of flight speeds and attitude angles. Based on the computed roots, the defined natural modes are similar on Earth and Mars, which consist of two stable subsidence modes and one divergence oscillation mode for each of the longitudinal and lateral motions. It is also revealed that since the real parts of the complex roots of the flight on Mars are positive, and only about 6% of those on Earth, its times of doubling the perturbations in the divergence oscillation modes take relatively longer than on Earth. For more details, the time-dependent responses of the Mars and Earth-flying robots are investigated under three initial non-dimensional disturbed translational speeds in the x-, y-, and z-axes. Overall, both FW flights on Mars and Earth are inherently unstable due to the divergence oscillation modes. However, the amplification of disturbances on Mars is significantly slower than on Earth due to their relatively smaller eigenvalues obtained from the EoMs for the Martian flight. Therefore, with the current design of the KUBeetle, when hovering on Mars, we may have enough time to stabilize the system using the feedback control, even though the robot is still dynamically unstable. The current study can be used to provide an insight into the controlled flight of tailless flapping-wing vehicles in the Martian atmospheric condition in the future, and generalized to similar flight in the atmospheres of other planets and their moons.

CRediT authorship contribution statement

Khanh Nguyen: Writing – review & editing, Writing – original draft, Visualization, Validation, Software, Methodology, Investigation, Formal

analysis, Data curation, Conceptualization. **Giheon Ha:** Software. **Taesam Kang:** Writing – review & editing, Validation. **Hoon Cheol Park:** Writing – review & editing, Supervision, Resources, Project administration, Investigation, Funding acquisition, Conceptualization.

Declaration of competing interest

The authors declare that they have no known competing financial interests or personal relationships that could have appeared to influence the work reported in this paper.

Data availability

The data that has been used is confidential.

Acknowledgement

This work is supported by the National Research Foundation of Korea (NRF) grant, funded by the Korea government (MSIT) (NRF-2022R1A4A101888411).

Appendix

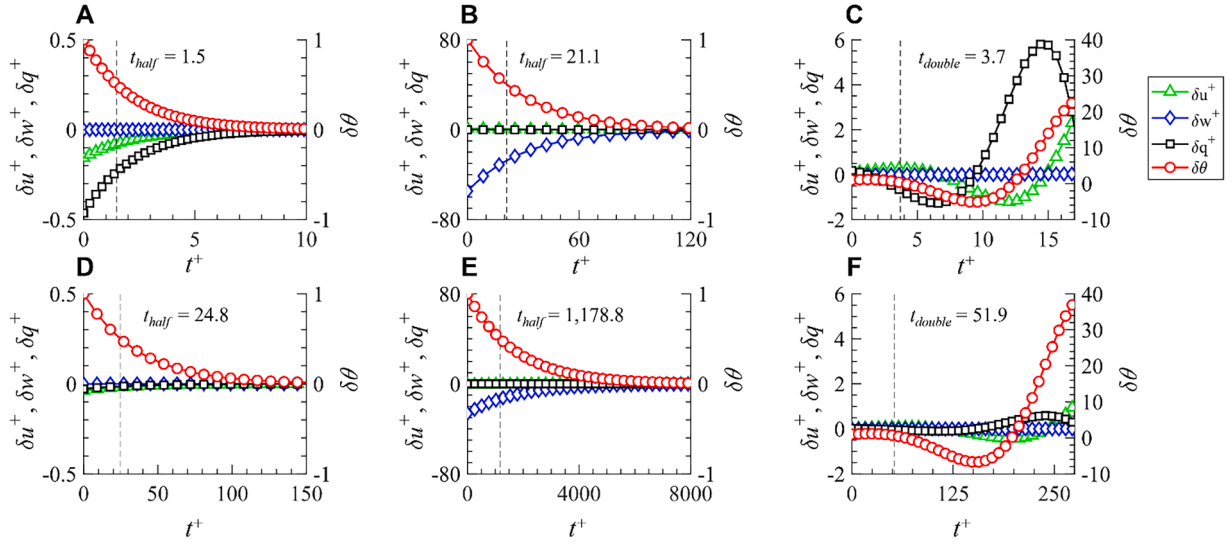

Fig. A. Non-dimensional longitudinal body state variables on (A)–(C) Earth [28] and (D)–(F) Mars, corresponding to the fast subsidence mode (A) & (D), slow subsidence modes (B) & (E), and divergence oscillation mode (C) & (F).

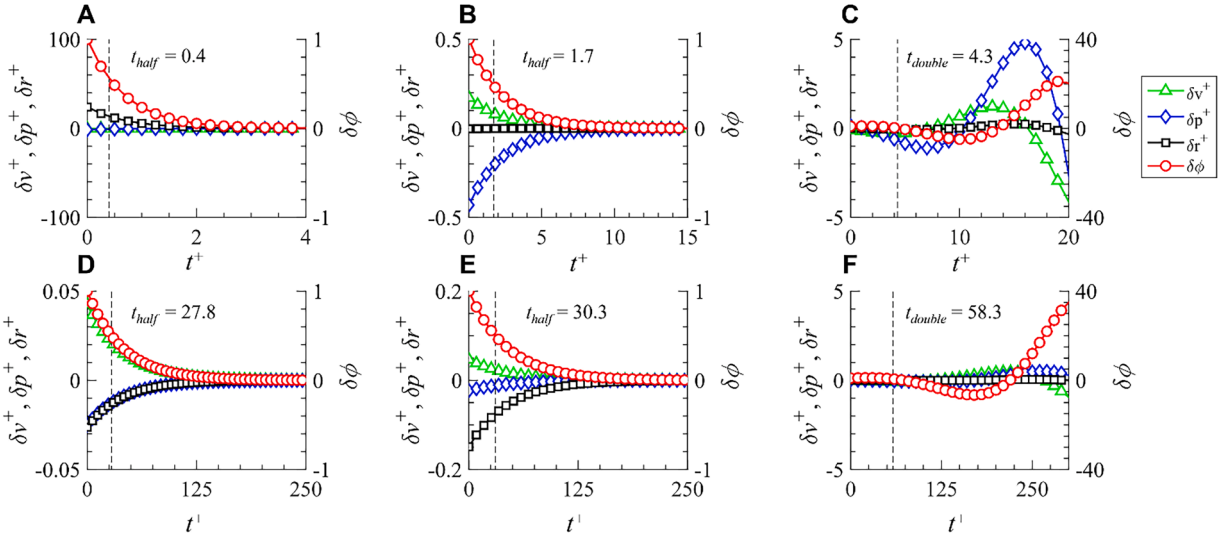

Fig. B. Non-dimensional lateral body state variables on (A)–(C) Earth [28] and (D)–(F) Mars, corresponding to the fast subsidence mode (A) & (D), slow subsidence modes (B) & (E), and divergence oscillation mode (C) & (F).

Table A
Dimensional longitudinal and lateral stability derivatives on Mars and Earth, and their fraction (Fr.).

	Longitudinal speed (u)-series			Vertical speed (w)-series			Pitch rate (q)-series		
	$X_u \times 10^{-2}$ [N.s.m^{-1}]	$Z_u \times 10^{-3}$ [N.s.m^{-1}]	$M_u \times 10^{-5}$ [N.s]	$X_w \times 10^{-4}$ [N.s.m^{-1}]	$Z_w \times 10^{-2}$ [N.s.m^{-1}]	$M_w \times 10^{-6}$ [N.s]	$X_q \times 10^{-4}$ [N.s]	$Z_q \times 10^{-4}$ [N.s]	$M_q \times 10^{-6}$ [N.m.s]
Earth	−2.392	−1.056	−83.037	2.787	−1.338	−16.466	6.219	1.154	−6.193
Mars	−0.168	−0.093	−6.550	0.944	−0.118	2.108	0.428	0.064	−0.382
Fraction (Fr.)	0.070	0.088	0.079	0.339	0.089	−0.128	0.069	0.055	0.062
	Yaw rate (r)-series			Roll rate (p)-series			Lateral speed (v)-series		
	$L_r \times 10^{-6}$ [N.m.s]	$Y_r \times 10^{-4}$ [N.s]	$N_r \times 10^{-5}$ [N.m.s]	$L_p \times 10^{-6}$ [N.m.s]	$Y_p \times 10^{-4}$ [N.s]	$N_p \times 10^{-6}$ [N.m.s]	$Y_v \times 10^{-2}$ [N.s.m^{-1}]	$L_v \times 10^{-4}$ [N.s]	$N_v \times 10^{-4}$ [N.s]
Earth	−8.026	2.488	−8.905	−5.697	−7.934	7.723	−2.662	6.529	1.368
Mars	0.269	0.115	−0.597	−0.641	−0.493	0.212	−0.191	0.527	0.044
Fraction (Fr.)	−0.034	0.046	0.067	0.113	0.062	0.027	0.072	0.081	0.032

(Note) The fractions (Fr.) in the shaded area appear in **Error! Reference source not found.**.

References

[1] BBC, (2022). https://www.bbc.com/news/science-environment-64002977.
[2] NASA, https://mars.nasa.gov/#red_planet/ (accessed August 8, 2023).
[3] NASA, (2021). https://mars.nasa.gov/technology/helicopter/#Overview.
[4] C.A. Kuhl, Mars aerial regional-scale environmental survey (ARES) coordinate systems definitions and transformations, Hampton, Virginia, 2009.
[5] NASAexplores, Mars plane flying, (2003). https://www.nasa.gov/audience/forstudents/9-12/features/nextstop_mars_feature_912.html (accessed August 8, 2023).
[6] "^?^(0) = ^!"count(descendant::ce:intra-ref)"^?^(0) = ^!"count(descendant::ce:doi)"^?^(0)[?pdftagstart "Link"] > L.A. Young, E.W. Aiken, M.R. Derby, R. Demblewski, J. Navarrete, Experimental investigation and demonstration of rotary-wing technologies for flight in the atmosphere of mars, in: Proceedings of the Annual Forum, Montreal, Canada, American Helicopter Society, American Helicopter Society, INC., 2002, pp. 268–284.
[7] W. Johnson, S. Withrow-Maser, L. Young, C. Malpica, W.J. Koning, W. Kuang, M. Fehler et al., Mars science helicopter conceptual design, No. ARC-E-DAA-TN78199 (2020).
[8] A. Colozza, R.C. Michelson, Planetary Exploration using Biomimetics, NASA Institute for Advanced Concepts, 2000.
[9] Y. Bar-Cohen, A. Colozza, M. Badescu, S. Sherrit, X. Bao, Biomimetic flying swarm of entomopters for mars extreme terrain science investigations, Concepts Approaches Mars Explor. 1679 (2012) 4075.
[10] R. Bardera, S. Sor, A. García-Magariño, Aerodynamics of mars 2020 rover wind sensors, in. Mars Exploration–A Step Forward, IntechOpen, 2020, https://doi.org/10.5772/intechopen.90912.
[11] T. Weis-Fogh, Quick estimates of flight fitness in hovering animals, including novel mechanisms for lift production, J. Exp. Biol. 59 (1973) 169–230, https://doi.org/10.1242/jeb.59.1.169.
[12] C.P. Ellington, The aerodynamics of hovering insect flight. IV. Aerodynamic mechanisms, Philos. Trans. R. Soc. Lond. B Biol. Sci. 305 (1984) 79–113, https://doi.org/10.1098/rstb.1984.0052.
[13] M.H. Dickinson, K.G. Götz, Unsteady aerodynamic performance of model wings at low Reynolds numbers, J. Exp. Biol. 174 (1993) 45–64, https://doi.org/10.1242/jeb.174.1.45.
[14] M.H. Dickinson, The effects of wing rotation on unsteady aerodynamic performance at low reynolds numbers, J. Exp. Biol. 192 (1994) 179–206, https://doi.org/10.1242/jeb.192.1.179.
[15] L. Chen, J. Wu, B. Cheng, Leading-edge vortex formation and transient lift generation on a revolving wing at low Reynolds number, Aerosp. Sci. Technol. 97 (2020) 105589, https://doi.org/10.1016/j.ast.2019.105589.
[16] B. Liang, M. Sun, Dynamic flight stability of a hovering model dragonfly, J. Theor. Biol. 348 (2014) 100–112, https://doi.org/10.1016/j.jtbi.2014.01.026.
[17] A.T. Nguyen, J.H. Han, A near-optimal-trim-search method for six-degrees-of-freedom model insects: an application to flight in the lateral-wind condition, Aerosp. Sci. Technol. 133 (2023) 108101, https://doi.org/10.1016/j.ast.2022.108101.
[18] M. Sun, J. Wang, Y. Xiong, Dynamic flight stability of hovering insects, Acta Mech. Sin. 23 (2007) 231–246, https://doi.org/10.1007/s10409-007-0068-3.
[19] M. Sun, Insect flight dynamics: stability and control, Rev. Mod. Phys. 86 (2014) 615–646, https://doi.org/10.1103/RevModPhys.86.615.
[20] J.K. Kim, J.S. Han, J.S. Lee, J.H. Han, Hovering and forward flight of the hawkmoth *Manduca sexta* : trim search and 6-DOF dynamic stability characterization, Bioinspir. Biomim. 10 (2015) 056012, https://doi.org/10.1088/1748-3190/10/5/056012.
[21] G.K. Taylor, A.L.R. Thomas, Dynamic flight stability in the desert locust Schistocerca gregaria, J. Exp. Biol. 206 (2003) 2803–2829, https://doi.org/10.1242/jeb.00501.
[22] M. Keennon, K. Klingebiel, H. Won, Development of the nano hummingbird: a tailless flapping wing micro air vehicle, in: Proceedings of the 50th AIAA Aerospace Sciences Meeting Including the New Horizons Forum and Aerospace Exposition, American Institute of Aeronautics and Astronautics, Reston, Virigina, 2012, https://doi.org/10.2514/6.2012-588.
[23] A. Roshanbin, H. Altartouri, M. Karásek, A. Preumont, COLIBRI: a hovering flapping twin-wing robot, Int. J. Micro Air Veh. 9 (2017) 270–282, https://doi.org/10.1177/1756829317695563.
[24] H.V. Phan, T.K.L. Au, H.C. Park, Clap-and-fling mechanism in a hovering insect-like two-winged flapping-wing micro air vehicle, R. Soc. Open Sci. 3 (2016) 160746, https://doi.org/10.1098/rsos.160746.
[25] H.V. Phan, H.C. Park, Mechanisms of collision recovery in flying beetles and flapping-wing robots, Science 370 (2020) 1214–1219, https://doi.org/10.1126/science.abd3285.
[26] H.V. Phan, S. Aurecianus, T.K.L. Au, T. Kang, H.C. Park, Towards the long-endurance flight of an insect-inspired, tailless, two-winged, flapping-wing flying robot, IEEE Robot. Autom. Lett. 5 (2020) 5059–5066, https://doi.org/10.1109/LRA.2020.3005127.
[27] L.T.K. Au, H.V. Phan, S.H. Park, H.C. Park, Effect of corrugation on the aerodynamic performance of three-dimensional flapping wings, Aerosp. Sci. Technol. 105 (2020) 106041, https://doi.org/10.1016/j.ast.2020.106041.
[28] K. Nguyen, L.T.K. Au, H.V. Phan, H.C. Park, Comparative dynamic flight stability of insect-inspired flapping-wing micro air vehicles in hover: longitudinal and lateral motions, Aerosp. Sci. Technol. 119 (2021), https://doi.org/10.1016/j.ast.2021.107085.
[29] K. Nguyen, L.T.K. Au, H.V. Phan, S.H. Park, H.C. Park, Effects of wing kinematics, corrugation, and clap-and-fling on aerodynamic efficiency of a hovering insect-inspired flapping-wing micro air vehicle, Aerosp. Sci. Technol. 118 (2021) 106990, https://doi.org/10.1016/j.ast.2021.106990.
[30] H.V. Phan, T. Kang, H.C. Park, Design and stable flight of a 21 g insect-like tailless flapping wing micro air vehicle with angular rates feedback control, Bioinspir. Biomim. 12 (2017) 036006, https://doi.org/10.1088/1748-3190/aa65db.
[31] H.V. Phan, S. Aurecianus, T. Kang, H.C. Park, KUBeetle-S: an insect-like, tailless, hover-capable robot that can fly with a low-torque control mechanism, Int. J. Micro Air Veh. 11 (2019) 175682931986137, https://doi.org/10.1177/1756829319861371.
[32] M. Karásek, F.T. Muijres, C. De Wagter, B.D.W. Remes, G.C.H.E. de Croon, A tailless aerial robotic flapper reveals that flies use torque coupling in rapid banked turns, Science 361 (2018) 1089–1094, https://doi.org/10.1126/science.aat0350.
[33] M. Karásek, M. Percin, T. Cunis, B.W. van Oudheusden, C. De Wagter, B.D. Remes, G.C. de Croon, Accurate position control of a flapping-wing robot enabling free-flight flow visualisation in a wind tunnel, Int. J. Micro Air Veh. 11 (2019) 175682931983368, https://doi.org/10.1177/1756829319833683.
[34] Q.V. Nguyen, W.L. Chan, Development and flight performance of a biologically-inspired tailless flapping-wing micro air vehicle with wing stroke plane modulation, Bioinspir. Biomim. 14 (2018) 016015, https://doi.org/10.1088/1748-3190/aaefa0.
[35] J. Zhang, F. Fei, Z. Tu, X. Deng, Design optimization and system integration of robotic hummingbird, in: Proceedings of the IEEE International Conference on Robotics and Automation (ICRA), IEEE, 2017, pp. 5422–5428, https://doi.org/10.1109/ICRA.2017.7989639.
[36] F. Fei, Z. Tu, J. Zhang, X. Deng, Learning extreme hummingbird maneuvers on flapping wing robots, in: Proceedings of the International Conference on Robotics

and Automation (ICRA), IEEE, 2019, pp. 109–115, https://doi.org/10.1109/ICRA.2019.8794100.
[37] M.E. Dillon, R. Dudley, Surpassing Mt. Everest: extreme flight performance of alpine bumble-bees, Biol. Lett. 10 (2014) 20130922, https://doi.org/10.1098/rsbl.2013.0922.
[38] M. Streinzer, J. Chakravorty, J. Neumayer, K. Megu, J. Narah, T. Schmitt, H. Bharti, J. Spaethe, A. Brockmann, Species composition and elevational distribution of bumble bees (Hymenoptera, Apidae, Bombus Latreille) in the East Himalaya, Arunachal Pradesh, India, Zookeys 851 (2019) 71–89, https://doi.org/10.3897/zookeys.851.32956.
[39] J.E. Bluman, J.A. Pohly, M.K. Sridhar, C. Kang, D.B. Landrum, F. Fahimi, H. Aono, Achieving bioinspired flapping wing hovering flight solutions on Mars via wing scaling, Bioinspir. Biomim. 13 (2018) 046010, https://doi.org/10.1088/1748-3190/aac876.
[40] C.K. Kang, F. Fahimi, R. Griffin, D.B. Landrum, B. Mesmer, G. Zhang, T. Lee, H. Aono, J. Pohly, J. McCain, M. Sridhar, Marsbee–swarm of flapping wing flyers for enhanced mars exploration, No. HQ-E-DAA-TN67472 (2019).
[41] S. Tsuchiya, H. Aono, K. Asai, T. Nonomura, Y. Ozawa, M. Anyoji, N. Ando, C. Kang, J. Pohly, First lift-off and flight performance of a tailless flapping-wing aerial robot in high-altitude environments, Sci. Rep. 13 (2023) 8995, https://doi.org/10.1038/s41598-023-36174-5.
[42] L. Wang, F.B. Tian, H. Liu, Numerical study of three-dimensional flapping wings hovering in ultra-low-density atmosphere, Phys. Fluids 34 (2022) 041903, https://doi.org/10.1063/5.0085021.
[43] A.E. Bryson, Control of Spacecraft and Aircraft, Princeton University Press, Princeton, 1993.
[44] B. Etkin, L.D. Reid, Dynamics of Flight: Stability and Control, John Wiley & Sons, 1995.
[45] B. Cheng, X. Deng, Translational and rotational damping of flapping flight and its dynamics and stability at hovering, IEEE Trans. Robot. 27 (2011) 849–864, https://doi.org/10.1109/TRO.2011.2156170.
[46] N. Gao, H. Aono, H. Liu, A numerical analysis of dynamic flight stability of hawkmoth hovering, J. Biomech. Sci. Eng. 4 (2009) 105–116, https://doi.org/10.1299/jbse.4.105.
[47] M. Karásek, Robotic Hummingbird: Design of a Control Mechanism for a Hovering Flapping Wing Micro Air Vehicle, Universite libre de Bruxelles, Bruxelles, Belgium, 2014.
[48] Z. Kamankesh, A. Banazadeh, Stability analysis for design improvement of bio-inspired flapping wings by energy method, Aerosp. Sci. Technol. 111 (2021) 106558, https://doi.org/10.1016/j.ast.2021.106558.
[49] Q.T. Truong, Q.V. Nguyen, V.T. Truong, H.C. Park, D.Y. Byun, N.S. Goo, A modified blade element theory for estimation of forces generated by a beetle-mimicking flapping wing system, Bioinspir. Biomim. 6 (2011) 036008, https://doi.org/10.1088/1748-3182/6/3/036008.
[50] Y. Xiong, M. Sun, Dynamic flight stability of a bumblebee in forward flight, Acta Mech. Sin. 24 (2008) 25–36, https://doi.org/10.1007/s10409-007-0121-2.
[51] L.T.K. Au, V.H. Phan, H.C. Park, Longitudinal flight dynamic analysis on vertical takeoff of a tailless flapping-wing micro air vehicle, J. Bionic Eng. 15 (2018) 283–297, https://doi.org/10.1007/s42235-018-0022-z.
[52] L.T.K. Au, H.C. Park, Influence of center of gravity location on flight dynamic stability in a hovering tailless FW-MAV: longitudinal motion, J. Bionic Eng. 16 (2019) 130–144, https://doi.org/10.1007/s42235-019-0012-9.
[53] G. Ha, H.C. Park, Aerodynamic and dynamic characteristics of flapping wings under low air density, Acta Astronaut (2024), https://doi.org/10.1016/j.actaastro.2024.06.048.
[54] H.F. Grip, W. Johnson, C. Malpica, D.P. Scharf, M. Mandić, L. Young, B. Allan, B. Mettler, M.S. Martin, J. Lam, Modeling and identification of hover flight dynamics for NASA's mars helicopter, J. Guid. Control Dyn. 43 (2020) 179–194, https://doi.org/10.2514/1.G004228.
[55] L.T.K. Au, H.C. Park, Influence of center of gravity location on flight dynamic stability in a hovering tailless FW-MAV: lateral motion, J. Bionic Eng. 17 (2020) 148–160, https://doi.org/10.1007/s42235-020-0012-9.
[56] MATLAB, Eigenvalues and eigenvectors - Eig, https://www.mathworks.com/help/matlab/ref/eig.html (accesed August 8, 2023).
[57] K. Atkinson, An Introduction to Numerical Analysis, John Wiley & Sons, 1991.